MARY KAY O'CONNOR PROCESS SAFETY CENTER
TEXAS A&M ENGINEERING EXPERIMENT STATION

20th Annual International Symposium
October 24-26, 2017 • College Station, Texas

Is my facility at risk? Understanding the risks associated with low burning velocity compounds

John Pagliaro, **Scott Davis** & Kees van Wingerden
GexCon US, Bethesda, Maryland, USA
sgdavis@gexcon.com

Abstract

A key factor when performing risk assessments and facility siting studies is to assess the explosion and flash fire risk of combustible fluids. There are accurate and established methods to do so when dealing with flammable fluids that have laminar burning velocities (LBVs) around 40 cm/s (e.g., most hydrocarbons). There is currently a need to establish equivalently accurate methods for mildly flammable fluids that have LBVs less than 10 cm/s (e.g., R-32 and ammonia). The use of such fluids is growing, particularly in the heating, ventilation, air conditioning, and refrigeration (HVAC&R) industries as the result of on-going efforts to phase out working fluids with high global warming potential.

Without an accurate method of assessing the explosion and flash fire risk of mildly flammable fluids, a very conservative approach is often applied. The approach is to assume the explosion properties of mildly flammable fuels are close to those of methane when evaluating the potential explosion consequences. This will, however, grossly over-predict the potential explosion consequences as flame speed and overpressures during explosions and flash fires are directly correlated to the LBV of the fuel. Furthermore, the likelihood of an explosion or flash fire may also be overpredicted when assuming flammability properties are equivalent to those of methane. Therefore, it is important to not only understand the explosion consequences but also the likelihood of having an explosion, which includes the probability of flammable mixtures forming and subsequently being ignited.

Flammability properties and characteristics of mildly flammable fluids must be thoroughly understood to accurately evaluate the probability and consequence of the fire/explosion hazards associated with their use. This study examines post-ignition consequences at large scales through experimentation and with computational fluid dynamics. Fundamental flammability properties of mildly flammable fluids are also measured and presented along with previously reported data in the literature to evaluate potential measurement uncertainties. The flammability properties are then discussed in the context of the likelihood of having an explosion or flash fire, specifically in regard to the probability of forming a flammable mixture and the probability of a flammable

mixture being ignited. The combined large-scale consequence testing, fundamental flammability and ignitibility experiments, and modeling results will allow for more accurate assessments of risk.

Keywords: *flammability properties, explosivity properties, low burning velocity gases, ammonia, R717, R32, mildly flammable gases*

1 Introduction

A key factor when performing risk assessments and facility siting studies is to assess the explosion and flash fire risk of combustible fluids. There are accurate and established methods to do so when dealing with highly flammable fluids that have laminar burning velocities (LBVs) around 40 cm/s (e.g., most hydrocarbons). There is currently a need to establish equivalently accurate methods for mildly flammable fluids that have LBVs less than 10 cm/s (e.g., R-32 and ammonia). The use of such fluids is growing, particularly in the heating, ventilation, air conditioning, and refrigeration (HVAC&R) industries as the result of on-going efforts to reduce human-induced global warming.

Without an accurate method of assessing the explosion and flash fire risk of mildly flammable fluids, a very conservative approach is often applied. The approach is to assume the explosion properties of mildly flammable fuels are close to those of methane when evaluating the potential explosion consequences. This will, however, grossly over-predict the potential explosion consequences as flame speed and overpressures during explosions and flash fires are directly correlated to the LBV of the fuel. Furthermore, the likelihood of an explosion or flash fire may also be overpredicted when assuming flammability properties are equivalent to those of methane. Therefore, it is important to not only understand the explosion consequences but also the likelihood of having an explosion, which includes the probability of flammable mixtures forming and subsequently being ignited.

To understand the actual large-scale risks associated with mildly flammable compounds, and to design effective mitigation measures, fundamental flammability characteristics must be well defined and consequences must be understood and demonstrated at representative scales. In addition, consequence tools such as computational fluid dynamics (CFD) models that can accurately predict post-ignition severity of events involving low LBV compounds ($\leq$ 10 cm/s) would serve as valuable tools for assessing risk and designing mitigation methods. Once a CFD model is validated against existing test data, it can then be used to explore the sensitivity of event severity to variables such as the properties of the flammable volume that forms from a leak, confinement, ventilation conditions, fuel reactivity and heat release, and safety mitigation measures.

This study presents the explosion consequences of ammonia and R32 as a representative mildly flammable compounds. Premixed methane/air mixtures are also presented to demonstrate the differences in the explosion consequences as compared to mildly flammable compounds. Results are presented for uncongested (low object density) and more congested regions along the flame path. The speed at which the flame burns and the resulting explosion severity is typically sensitive to congestion levels along the flame path [1]. Fundamental flammability properties are also prvided for ammonia and other mildly flammable fluids and are: (1) compared to existing data in literature; (2) compared to the properties of methane to further examine the differences in risk, particularly in terms of ignition probability; and (3) coupled with the large-scale results to see whether large-scale consequences correlate with lab-scale properties. The properties measured and presented include upper and lower flammability limits (LFL and UFL), auto-ignition temperature (AIT), minimum ignition energy (MIE), explosion severity index (K_g), peak pressure rise (ΔP_{max}), and burning velocity as a function of equivalence ratio.

The main goal of the study is to assess the accuracy of the computational fluid dynamics models for predicting post-ignition event severity for tests performed in the 50 m^3 rig. The 50 m^3 rig experiments were modeled with the CFD package FLACS and the predicted deflagration overpressures are compared to the measurements. The desired outcome is that the combined results from this study will enable a more accurate assessment of risks, which can be compared directly to the risks for highly flammable fluids, and which can serve as the basis for establishing proper mitigation measures.

2 Experimental

2.1 Lab-scale

Four different standard experiments provided the combustion properties of ammonia and methane. The lower and upper explosion limits (LEL and UEL) were determined using the EN-1839 method [2]. Mixtures were prepared in a 2 L cylindrical vessel equipped with a pressure transducer and small polycarbonate windows for visual monitoring of ignition and flame propagation. Test mixtures were subjected to a 15 kV oscillating spark across centrally located electrodes. Once a flammable mixture was identified, tests were repeated at higher and lower fuel concentrations until the pressure rise for a given mixture was negligible (below the 50 mbar threshold).

Auto-ignition temperature (AIT) was determined using the EN-14522 method [3]. Fuel/air mixtures were injected into a 200 mL narrow-necked Erlenmeyer flask placed in a temperature-controlled oven. The test operator monitored the flask for 5 minutes to see if a flame established, and the lowest oven temperature for which a flame did established was recorded as AIT.

Minimum ignition energy (MIE) was determined using the ASTM E582 method [4]. Tests were performed in a 2 L cylindrical vessel equipped with a small polycarbonate viewing window. For each test, ignition sparks were generated using one of two circuits, depending on the expected MIE. When the expected MIE was low, a standard capacitive discharge circuit was used. The spark energy was calculated from the capacitance of the circuit and the measured voltage, and for this circuit, the energy could be set as low as 0.1 mJ, which is on the order of the MIE for common hydrocarbons such as methane and propane [5]. When the expected MIE was higher (which is the case for mildly flammable compounds), ignition was attempted with an alternative ignitor capable of generating energies greater than 1.6 mJ. The ignition system used a moderately high voltage power supply (30 kV) and a transformer which created a trigger spark that broke down the spark gap. Mixtures were subjected to sparks with increasing energy until ignition was observed through the viewing window.

Experiments in a 20 L semi-spherical vessel provided the explosion pressure (constant-volume) as a function of time. Further processing of the data yielded the maximum pressure rise p_{max}, the deflagration index K_g, and the laminar burning velocity S_u. The test apparatus is a replica of the Bureau of Mines apparatus described in ref. [6].

Reactant mixtures were prepared in the chamber using the partial pressure method. A 15 kV oscillating spark ignitor (similar to the ignitor used for the explosion limit tests) created a 0.2 s duration spark across a gap between two electrodes at the center of the chamber. The explosion pressure was recorded with two piezo-electric pressure transducers (Kistler 701A) located on

opposite sides of the chamber. While consistently very similar, the two signals were averaged to yield the maximum pressure rise Δp_{max} and the maximum rate of pressure rise dp/dt_{max}. From dp/dt_{max}, the deflagration index K_g was determined using Eq. 1, where V is the vessel volume (20 L):

$$K_g = dp/dt_{max} * V^{1/3} \quad (1)$$

Burning velocities S_u were determined from the pressure traces of the quiescent tests by applying the expression derived by Lewis & von Elbe,

$$S_u = (R/3)\left[1 - (1 - y_b)(p_0/p)^{1/\gamma_u}\right]^{-2/3} (p_o/p)^{1/\gamma_u}(dy_b/dt) \quad (2)$$

where R is the chamber radius, p_0 is the initial pressure, p is the instantaneous chamber pressure, γ_u is the specific heat ratio, and y_b is the instantaneous mass fraction of burned gas in the chamber. Instead of assuming the linear relationship between y_b and p proposed in ref. [7], the present work applies the thermodynamic model described in ref. [8].

2.2 50 m³ rig

The large-scale test rig is rectangular with an aspect ratio of 3.2 and an internal volume of 50 m^3. For each test, premixed reactants are prepared in the rig at the concentrations resulting in the maximum burning velocity (i.e., slightly rich conditions). The gases are ignited and the severity of the ensuing deflagration is monitored via pressure measurements and high speed video. As illustrated in Figure 1, the rig is 8 m long, 2.5 m tall, and 2.5 m wide with a clear polycarbonate panel along the front so that the deflagration can be filmed. The frame, floor, ceiling, back wall, and one end wall (west end) are made of steel, and the east end is left open for venting. Tests are performed with the partially confined rig with two levels of object density: (1) empty where the only obstructions inside the rig were four horizontal beams located every 2 m at mid-height to provide structural support; and (2) congested where additional objects were added to module as shown in Figure 2. An AC transformer generates a spark to initiate reaction. As seen in Figure 1 and Figure 2, the ignition transformer is located 1 m from the closed end, 1.25 m from the front wall (centered along the width), and 1.35 m above the floor.

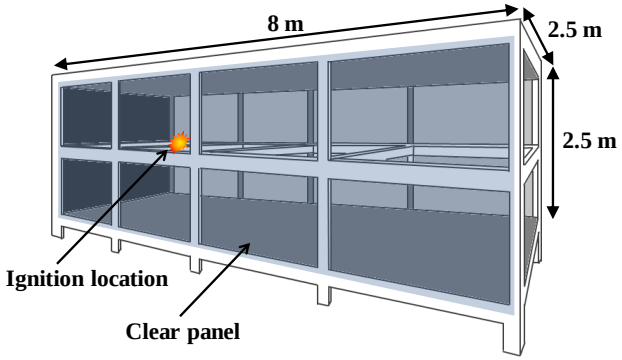

Figure 1: 50 m³ test rig in the empty configuration.

Figure 2: 50 m^3 test rig in the congested configuration.

2.2.1 Instrumentation

Internal pressures are monitored with eight piezo-electric pressure transducers (Kistler 7261) that have a 13 kHz response and are connected to a charge amplifier (Kistler 5011A). The eight sensors are aligned in rows of four along the floor near the rear wall and along the ceiling down the center of the rig (mid-depth). The external pressure along the vent path (i.e. the blast wave pressure) is monitored with three skimmer plate transducers that are connected to a separate charge amplifier (Kistler 4601). The sensors are position 4 m, 8 m, and 12 m from the end of the enclosure at mid-depth and mid-height. The sensor locations are shown in Figure 3, with the x, y, and z directions defined. The signals from each sensor are filtered with a low pass filter at 1000 Hz to remove extremely short pressure peaks that are likely caused by reflections inside the sensors [9].

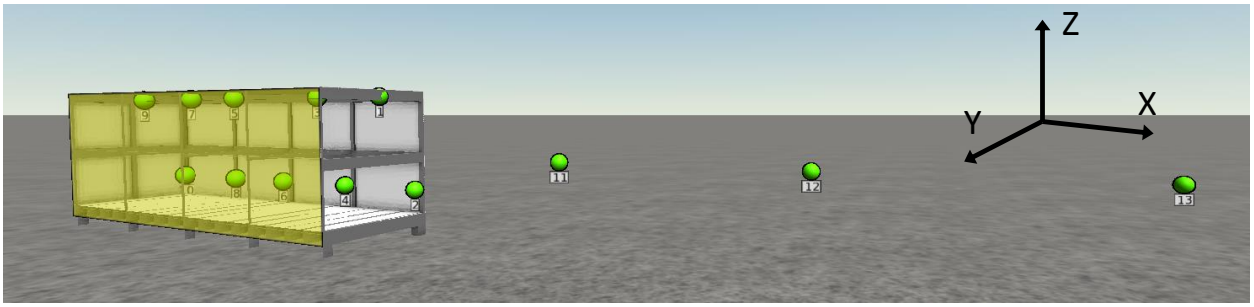

Figure 3: Pressure sensor locations shown by the green circles.

Experiments are recorded with two high-speed digital cameras (Edgetronic), each having a maximum frame rate of 1800 fps. The cameras are triggered just prior to ignition, along with a light mounted on the outside of the rig that provides ignition timing in the videos.

2.2.2 Procedure

For each test, the rig is filled with a homogeneous mixture of fuel and air. In order to prepare the mixture in the rig, the open end is first sealed with a thin plastic sheet. Fuel is added at five different locations to help ensure uniform distribution, and a re-circulation system provides mixing with a centrifugal fan. During mixture preparation, a multi-channel suction system removes mixture samples that are analyzed using an infrared gas analyzer (Servomex 4200) and an oxygen analyzer (Servomex Xendos 225) to check the constituent concentrations. Once the target concentrations are met and mixing is complete, two 8” butterfly valves are closed to isolate the

mixing system from the rig, the thin plastic sheet covering the vent is released, and the data acquisition and ignition are triggered.

3 Numerical Methods

FLACS is used in the present study to simulate the large-scale ignition tests. FLACS is a computational fluid dynamics (CFD) tool used extensively in the Oil & Gas and chemical industries to predict dispersion of accidental releases and the consequences of vapor cloud deflagrations. FLACS can predict several transient features of a deflagration including overpressure, pressure impulse, and flame dynamics. These physical phenomena are simulated in a three-dimensional domain while taking into account the interaction between the fluid flow and obstacles, obstructions, and topography.

FLACS solves the compressible Reynolds-Averaged Navier–Stokes (RANS) equations on a 3D Cartesian grid using a finite volume method. Incorporated in the model are the conservation equations for mass, impulse, enthalpy, turbulence and species, with the equations closed by invoking the ideal gas law and the standard k-ε turbulence model [10, 11]. FLACS uses a flamelet-based combustion sub-model with one-step reaction kinetics characterized by the laminar burning velocity of the fuel/air mixture, which is specified in FLACS as a function of equivalence ratio, temperature, and pressure. To model combustion and explosion dynamics, a flame growth sub-model describes how the local flame speed changes with the above-mentioned parameters as well as the turbulence characteristics of the flow field. Then, using sub-grid models, the real flame area is properly described and corrected for curvature at smaller scales than the grid. Furthermore, FLACS accounts for flame acceleration due to flame instabilities, flame-folding by obstacles, and turbulent mixing [12, 13].

FLACS captures the effect of small obstacles while remaining computationally tractable by implementing a "distributed porosity concept" [1]. Large geometries are modeled on a Cartesian grid with larger objects and walls represented on-grid, and smaller objects represented sub-grid. Each grid volume has an assigned volume porosity, area porosity, and drag coefficient based on the congestion contained within the grid cell. The drag from partially blocked cells is then accounted for in the RANS equations through a modified turbulence generation rate term in the k-ε turbulence model. With this approach, small objects contribute to flow resistance, turbulence generation, and flame folding without needing to be fully resolved by the grid.

Figure 4 provides the FLACS geometries for the empty and congested rig simulations. Pressure monitoring points were specified where the pressure transducers were located in the experiment. A uniform 10 cm grid maps the computational domain within the rig and out toward the last far field sensor (12 m from the open end). A coarser grid maps the remainder of the computational domain, which extends 10 m in each direction to minimize the influence of non-physical boundary reflections. PLANE_WAVE boundary conditions are specified to further reduce boundary interactions as recommended by Hansen et al. [9].

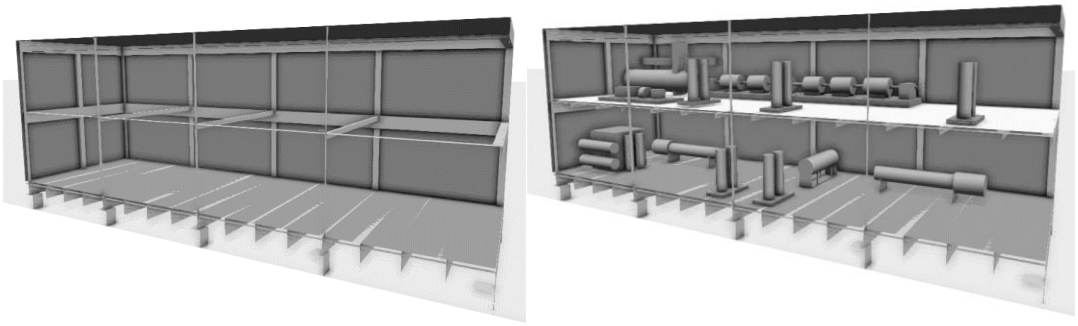

Figure 4: FLACS model of the 50 m^3 rig in the empty (left) and congested (right) configuration.

FLACS is used extensively to simulate liquid and vapor dispersion in addition to simulating ignition events. Both the probability and severity of an ignition event depend on how ammonia disperses within the space where it is leaked as this controls the characteristics of the flammable cloud that forms. Example characteristics include the size and location of the flammable cloud and the concentration of ammonia within it. Ammonia is unique among refrigerants as it is less dense than air and therefore, depending on how it is releases, can accumulate along the ceiling, whereas most other refrigerants are denser than air and accumulate along the floor. FLACS accounts for variations in fluid density and therefore accurately predicts where released refrigerants may accumulate.

4 Results and Discussion

4.1 Flammability and ignitability properties of mildly flammable fluids

The flammability properties for ammonia/air determined in the present study and presented previously in literature [14-18] are provided in Table 1. The measured LEL, UEL, AIT, and P_{max} values are close to previously reported results. Larger scatter exists in the MIE data, with the measured value close to the lower end of the experimentally determined range. The present K_g value is somewhat lower than reported in NFPA 68.

Table 1: Flammability and ignitability properties of <u>ammonia</u>.

Source	LEL %v/v	UEL %v/v	AIT (°C)	MIE (mJ)	ΔP_{max} (bar)	K_g (m*bar/s)
Present Study	15.8	32.4	637 ± 5	15-20	4.4	6
Minor and Spatz 2008	15	28		100		
Kondo et al. 2006	15.2	30				
Ronneyand Wachman 1985	14	32.2				
Airgas SDS	15	28	651			
Verkamp et al. 1967				14		
Takizawa et al. 2015 (calculated)				45		
NFPA 68 1998 Edition					4.4	10

Table 2 provides flammability properties for R32/air measured in the present study and reported in literature [19-21]. The measured LEL and UEL are similar to previous measurements. The present AIT is somewhat lower than listed in the Airgas MSDS and the MIE is close to the JSRAE

value and about half of the value measured by Minor et al. [22] and calculated by Takizawa et al. [18].

Table 2: Flammability and ignitability properties of R32.

Source	LEL %v/v	UEL %v/v	AIT (°C)	MIE (mJ)	ΔP_{max} (bar)	K_g (m*bar/s)
Present Study	13	29.6	483 ± 4	13.5 ± 1.5	7.2	14
Jabbour and Clodic 2004	14.4	29.3				
Kondo et al. 2004	13.3	27.5				
Richard and Shankland 1992	13	29				
Daikin msds	13.8	29.9				
Airgas msds	13	33	530			
Minor and Spatz 2008	14.4	29.3		30		
JSRAE 2012 progress report				15		
Takizawa et al. 2015 (calculated)				29		

Overall, the flammability properties for ammonia and R32 are fairly well established. Additional work is required to reduce the uncertainty in the MIE, which is known to typically have the largest measurement uncertainty considering the sensitivity to test setup [18] and the difficulty in quantifying the actual energy transferred to the flammable mixture as opposed to that discharged from a capacitor or even measured across the electrode gap [23].

4.1.1 General LBV observations

Figure 5 provides the measured burning velocities for ammonia/air and R32/air as a function of equivalence ratio Φ, together with previously published data [19, 24-29]. The results are presented as-determined and shifted to compensate for the adsorbing nature of ammonia on the inner surfaces of the test vessel (as done in ref. [24]). The "shifted" results in Figure 5 are only an estimate and based on equivalence ratios corresponding to 95% of the recorded ammonia volume fraction for each test. The measured maximum burning velocity $S_{u,max}$ for ammonia/air and R32/air was 7.5 cm/s and 6.7 cm/s respectively, which are very close to $S_{u,max}$ reported in previous studies . For ammonia/air, the burning velocity peaks at rich conditions ($\Phi \approx 1.1$) and drops to about 80% of the peak value at $\Phi = 1.0$ and 1.25 (for the shifted results). For R-32/air, the burning velocity is relatively constant for $1.0 \geq \Phi \geq 1.27$, and drops off considerably to 72% of the peak value at slightly lean conditions ($\Phi = 0.9$). In general, the present burning velocities are within the scatter of previously published results and the data comparison shows sufficient agreement for $S_{u,max}$.

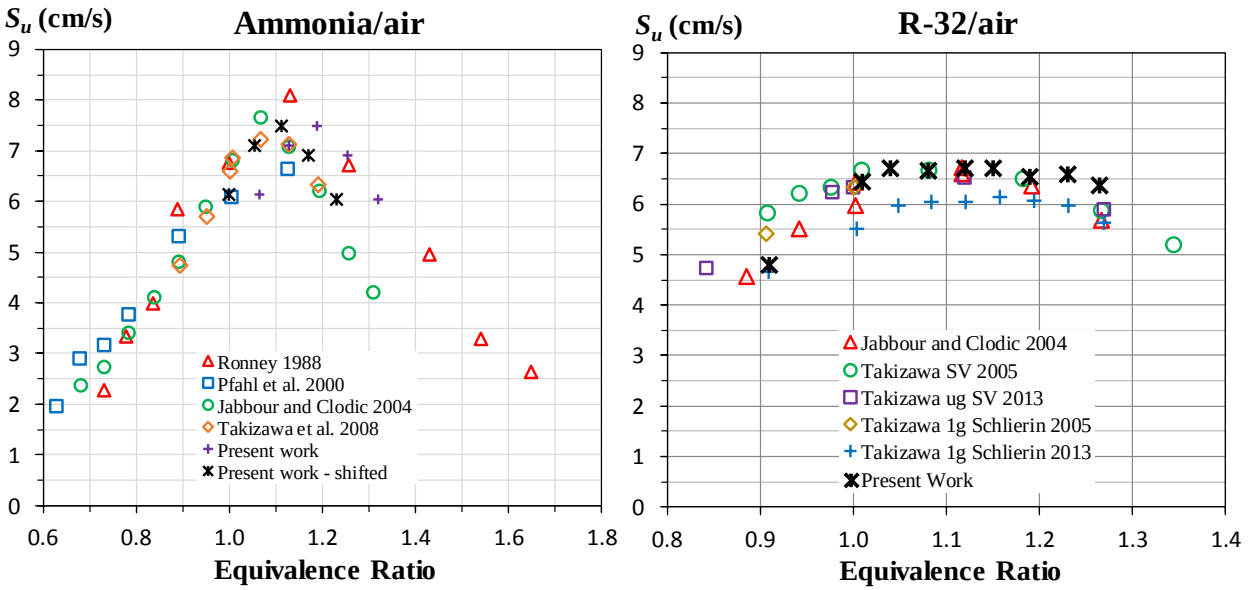

Figure 5: Comparison of present and previously reported burning velocities of ammonia/air (left frame) and R32/air (right frame) as a function of equivalence ratio.

4.1.2 Risk probability based on flammability properties

The flammability properties LEL, AIT, and MIE are used to assess the probability of an ignition event. The LEL establishes the likelihood of forming a flammable mixture (i.e., the higher the LEL the less likely a flammable cloud will form) and AIT and MIE establish the likelihood of ignition in addition to which types of ignition sources are sufficient. The properties P_{max}, K_g, and S_u govern the resulting deflagration consequences after ignition. S_u and K_g are direct and indirect measures of reactivity respectively, and P_{max} is an indicator of the energy release and pressure realizable during a constant volume event. By comparing these properties for ammonia and methane, we can begin to differentiate between the risks associated with each.

Table **3** compares the flammability properties of methane, ammonia, and R32 measured in the present study. The higher LEL for ammonia and R32 means they have a lower probability of forming a flammable mixture compared to methane. The higher MIE and AIT for ammonia also mean it has a lower likelihood of ignition. For R32, the higher MIE, but lower AIT means that the probability of ignition compared to that of methane depends on the types of distribution of ignition sources present in a particular scenario. The lower P_{max}, K_g, and $S_{u,max}$ for ammonia and R32 suggest less severe consequences from a resulting deflagration event. Presented next are large-scale tests showing the actual consequences of partially confined deflagrations involving mildly flammable and highly flammable substances, with ammonia and methane results presented as representative fluids for each class respectively.

Table 3: **Flammability and ignitability properties the highly flammable fluids, methane and propane, and for the mildly flammable fluids, ammonia and R32.**

Reactant	LEL (% vol)	UEL (% vol)	MIE (mJ)	AIT (°C)	$\Delta P_{max,Quies}$ (bar)	$K_{g,Quies}$ (m*bar/s)	$S_{u,max}$ (cm/s)
Methane	4.6	15.4	0.24-0.27	537	7.6	65	37.0
Ammonia	15.8	32.4	15-20	637	4.4	6	7.5
R32	13.0	29.6	12-15	483	7.2	14	6.7

4.2 50 m^3 rig tests

Experiments in a partially confined 50 m^3 test rig provided consequence data for methane/air and ammonia/air post-ignition events. A high-speed camera filmed the events and pressure transducers recorded overpressures. The following sections discuss the primary differences in the experimental results.

4.2.1 Flame dynamics

Figure 6 shows the initial flame development of near-stoichiometric ammonia/air (top) and methane/air (bottom) for tests without congestion. Note that the background is darker in the methane test because the recording frame rate was higher and the test was done later in the day. In Figure 6, the left-most column of images shows the initial flame after ignition, and the time from this point on is provided in the bottom corner of all subsequent images. While both flames start off nearly spherical, the ammonia flame propagates much slower than the methane flame. For methane/air, the diameter of the flame sphere grows much faster than for ammonia/air and the center remains roughly stationary in the z-direction. The high reactivity of methane/air results in flame front velocities that are much faster than the buoyancy driven flow, hence the flame dynamics are dominated by the convective "push" of the expanding burned gases behind the flame. In contrast, the ammonia/air flame starts off spherical and rises toward the ceiling. A dimple gradually forms at the base of the flame sphere as the upward motion outpaces the downward flame propagation. When the ammonia flame reaches the ceiling, the dimple has extended nearly half-way through the flame and the flame shape is closer to a mushroom cap instead of a sphere.

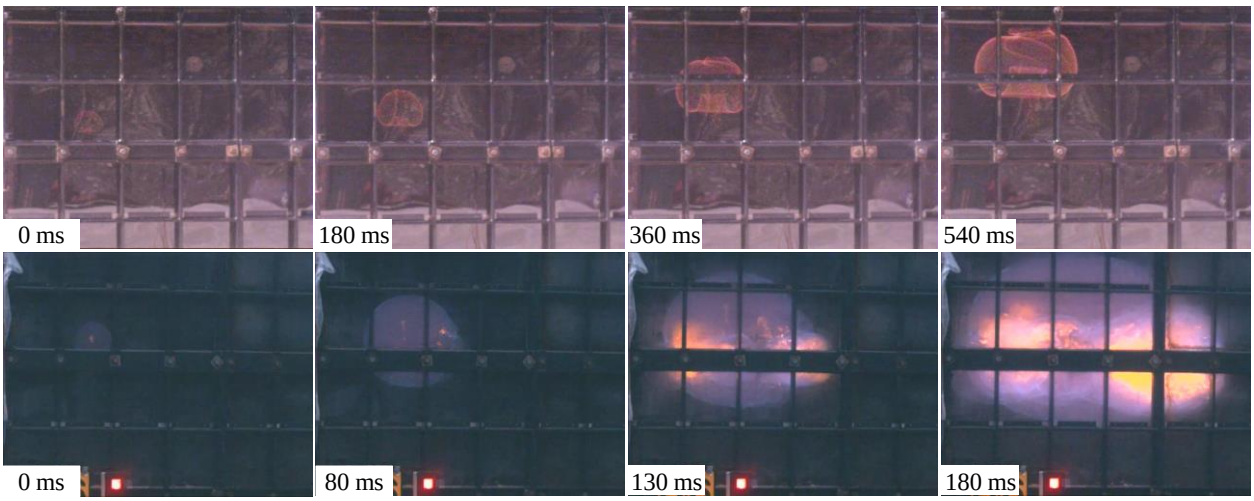

Figure 6: Flame dynamics of ammonia/air (top) and methane/air (bottom) during the initial flame development in the tests without congestion. The time for the flame to progress to the current state, in relation to the initial state seen in the first row of images is provided in the bottom corner.

Initial flame propagation during the R32/air test in the empty rig was similar to the propagation observed for ammonia/air up until the flames first contacted the ceiling. Once this occurred, the R32/air flame experienced partial quenching once it contacted the ceiling, and thus didn't start propagating horizontally along the ceiling until roughly 2 seconds after the ammonia/air flame. This is shown in Figure 7, which compares the flame propagation of R32/air and ammonia/air after contacting the ceiling.

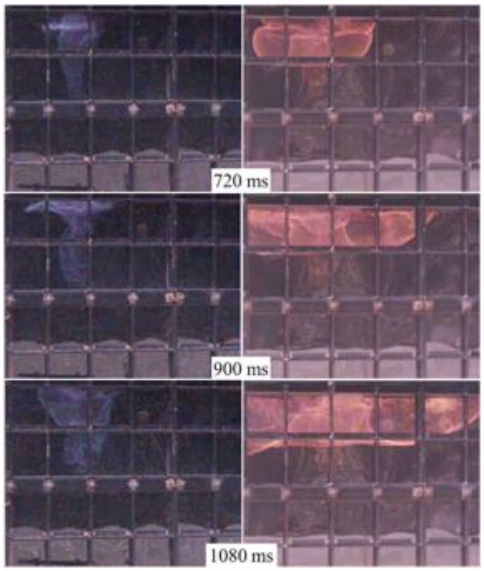

Figure 7: Flame propagation of R32/air and ammonia/air after first contact with the ceiling of the test rig.

The flame dynamics of high burning velocity fuels such as methane ($S_u \approx 40$ cm/s) and low burning velocity fuels such as ammonia ($S_u < 10$ cm/s) were not only different during the initial flame development, but also during the latter stages of propagation. Figure 8 shows methane/air (left frames) and ammonia/air (right frames) flames as they propagate throughout the empty rig. The methane/air flame starts off spherical and smooth, and because of the higher burning velocity, spherically expands in all directions until the flame front reaches the back, top and bottom walls. The expanding burned gases continue to convectively "push" the flame front horizontally towards the open end as it consumes the entire reactant mixture, further contributing to the heat release and horizontal expansion.

The flame dynamics are much different for a near-stoichiometric mixture of ammonia/air, which has a burning velocity ≈ 7 cm/s. The flame sphere is driven upward and contacts the ceiling when the flame diameter is about 2 m. The flame then spreads along the ceiling and its movement is controlled by the buoyancy driven flow of the burned gas (i.e., hot combustion products). Once the leading edge of the flame reaches the vent opening, the flame begins to slowly propagate downward as a very smooth and well-defined flame surface. Note that the overall flame dynamics of R32 were similar to the dynamics observed for ammonia, although the R32 flame experienced a higher degree of quenching when it first contacted the ceiling of the test rig (see ref. [30] for

more details). As a result, the R32/air flame reached the opening of the test rig roughly 2 seconds later than the ammonia/air, however flame propagation was similar once the horizontal spread along the ceiling started.

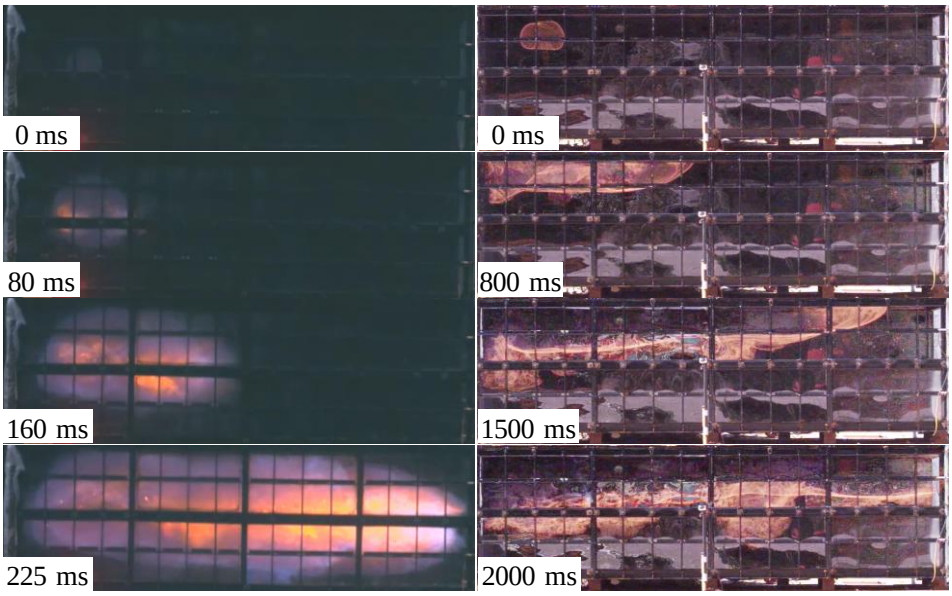

Figure 8: Flame dynamics of methane/air (left) and ammonia/air (right) in the 50 m^3 rig <u>without</u> added congestion.

Images of the methane/air (left frames) and ammonia/air (right frames) tests in the congested rig are shown in Figure 9. Even with added congestion in the rig, the ammonia/air flame starts off buoyancy driven. Notice that the ammonia flames in the first two images are similar to the flames observed during the test with no congestion. The flame rises and propagates along the ceiling until enough congestion induced turbulence is generated ahead of the flame front to sufficiently increase the flame speed. While the methane/air flames in the congested and empty tests are both convectively driven flows, the additional congestion creates turbulence and the flame front is much more wrinkled in the congested case as it propagates through the rig (compare images in Figure 8 and Figure 9).

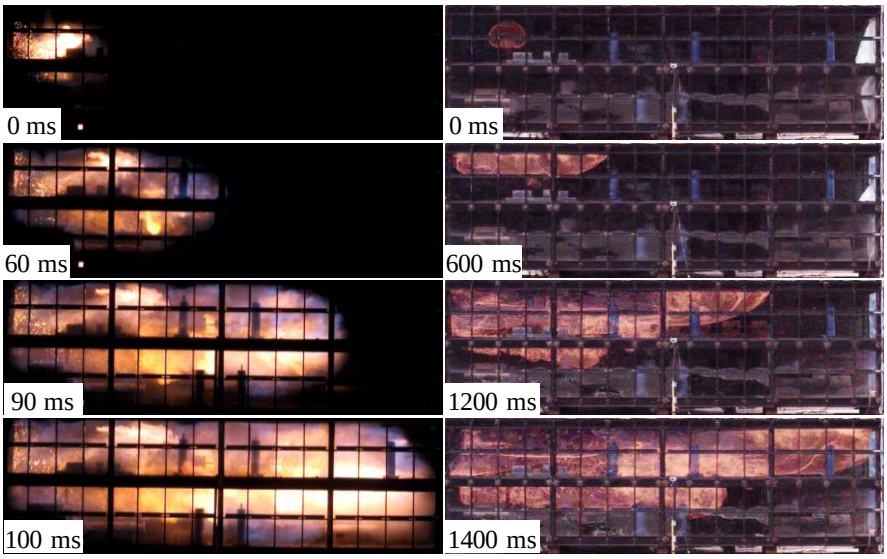

Figure 9: Flame dynamics of methane/air (left) and ammonia/air (right) in the 50 m^3 rig with added congestion.

When low burning velocity fuels are premixed in air, flame propagation is initially dominated by buoyancy and if no confinement is present, may result in negligible overpressures. However, if confinement and congestion are present the consequences from low burning velocity fuels can be orders of magnitude higher. Therefore, methods of accurately predicting the consequences of events involving these fuels must therefore not only take into account buoyancy effects during early flame propagation but also the flame acceleration effects in the event confinement and congestion are present. As shown in an upcoming section, preliminary comparisons of FLACS predictions with experimental results show that FLACS accurately predicts the flame dynamics of slow burning flames, and the explosion consequences can differ by orders of magnitude depending on the actual plant or building specifics.

4.2.2 Overpressures

A primary hazard of deflagrations is the overpressure they create. Figure 10 compares overpressure generated from methane, ammonia, and R32 deflagrations in the empty and congested rig configuration. In general, overpressures generated in the ammonia and R32 tests are 1-2 orders of magnitude less than overpressures generated in the methane tests. Peak overpressures within the rig were around 0.1 kPa and 1 kPa for the empty and congested test with ammonia and R32. Conversely, methane tests in the empty and congested rig resulted in peak internal pressures near 10 kPa and 25 kPa respectively. Decaying external overpressures were registered during the ammonia and R32 tests in the congested rig, and were again orders of magnitude lower than the external overpressures registered during the methane tests. No external overpressures were registered during the ammonia or R32 test in the empty rig because the pressures waves either dissipated before reaching the first external sensor or they reached the sensors after the data acquisition system stopped recording (set to record for 3 s after ignition). Note that during the R32 test in the empty configuration the data acquisition stopped recording before the flame front reached the end of the test rig (because of the delayed flame propagation after partially quenching at the ceiling) and therefore it is possible that the actual internal peak pressures were higher than what is reported in the figure below.

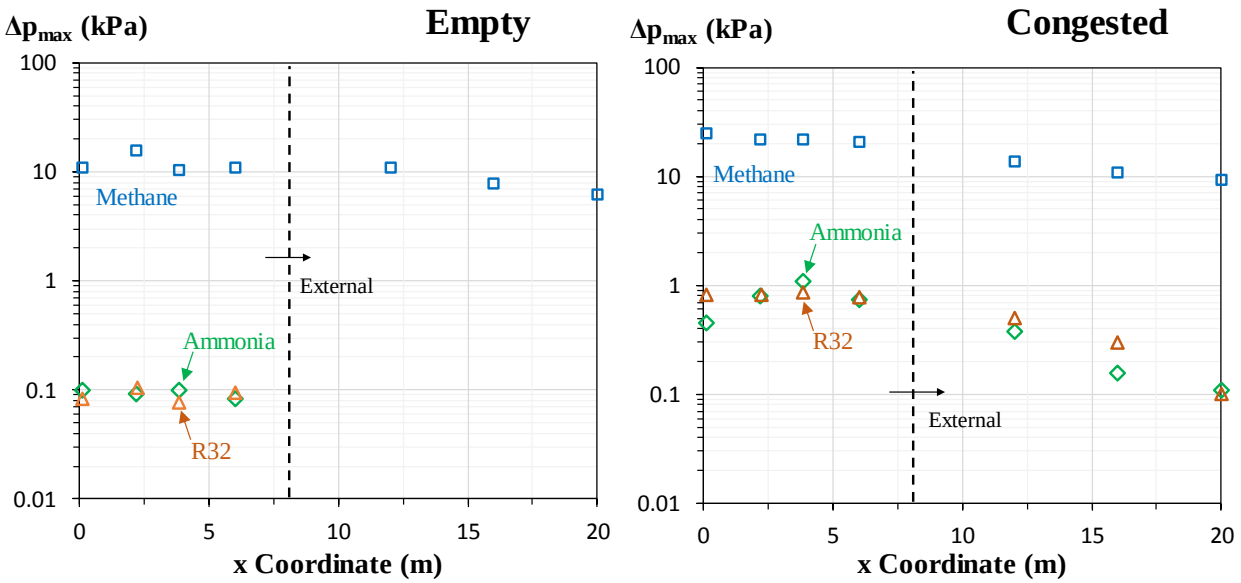

Figure 10: Deflagration overpressures measured within and outside the test rig during tests with methane, ammonia, and R32 in the empty (left image) and congested (right image) test configuration.

4.3 FLACS modeling

Ammonia tests in the 50 m^3 rig were modeled in FLACS and the predicted flame dynamics and overpressures are compared to experimental observations below. FLACS predictions with methane have been extensively validated (e.g., in ref. [9]) and therefore only validation for ammonia and R32 is discussed. Figure 11 compares the flame dynamics for the ammonia test in the empty rig. The FLACS images show gases at or above 2000 K (i.e. the burned gases), therefore the outer edges of the colored cloud are the flame front. In each row of images is the elapsed time from the first row of images. The evolution of the predicted ammonia flame is similar to what was observed during the experiment. Buoyancy drives the initial flame upward and then the flame expands across the ceiling of the rig. Once the flame front exits the rig, it begins to burn slowly downward throughout the rig. While the flame propagation is slightly faster in the FLACS simulation (through comparison of image time stamps), FLACS captures buoyancy aspects that become increasingly important for low burning velocity fuels. Note that FLACS predicted similar flame dynamics for R32 as it did for ammonia since the laminar burning velocities are similar. FLACS did not predict the partialflame quenching that occurred for R32 as there are no quenching sub-models in the software. Therefore, the predicted flame front in FLACS reached the open end of the test rig earlier than observed in the test.

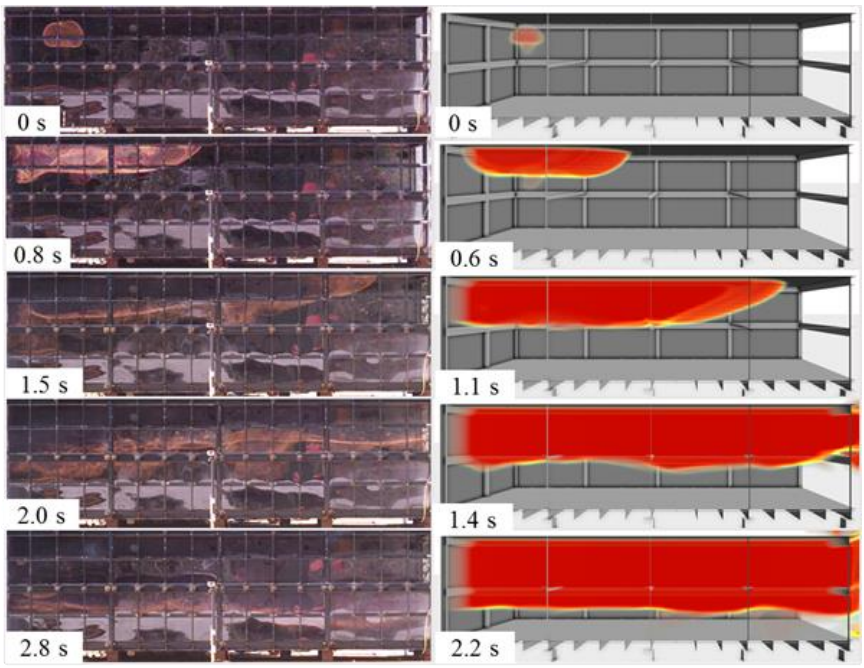

Figure 11: Comparison of flame dynamics observed in experiments and predicted in FLACS for ammonia tests in the <u>empty</u> rig.

Figure 12 compares the FLACS predictions to experimentally observed flame dynamics during the ammonia test in the congested rig. Agreement between the two is similar to what was observed for tests in the empty rig. Images of the experiment show that the flame is more wrinkled as a result of the interaction with the various obstacles in the rig. The flame is also more wrinkled in the FLACS simulation compared to the simulations results for the empty rig test. The time stamps on each image show that the flame in the FLACS simulation propagates slightly faster than the flame in the experiment.

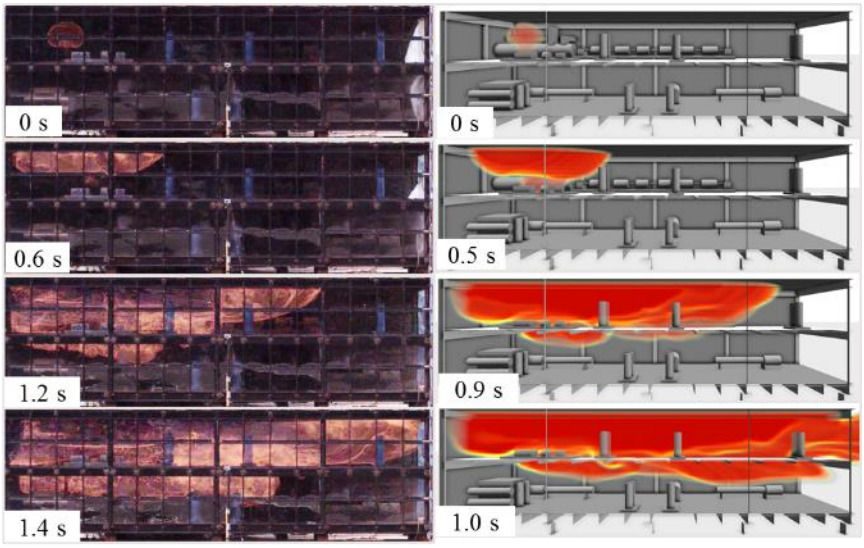

Figure 12: Comparison of flame dynamics observed in experiments and predicted in FLACS for ammonia tests in the <u>congested</u> rig.

Figure 13 compares the predicted and measured overpressures for ammonia/air in both the uncongested and congested rig configuration. The results shown are the average of the pressures at the ceiling and floor sensors at each location along the x-direction (refer to Figure 3 for sensor locations). FLACS predictions were generally in good agreement with the experimental values, with overpressures being slightly over-predicted in the empty configuration and under-predicted in the congested configuration.

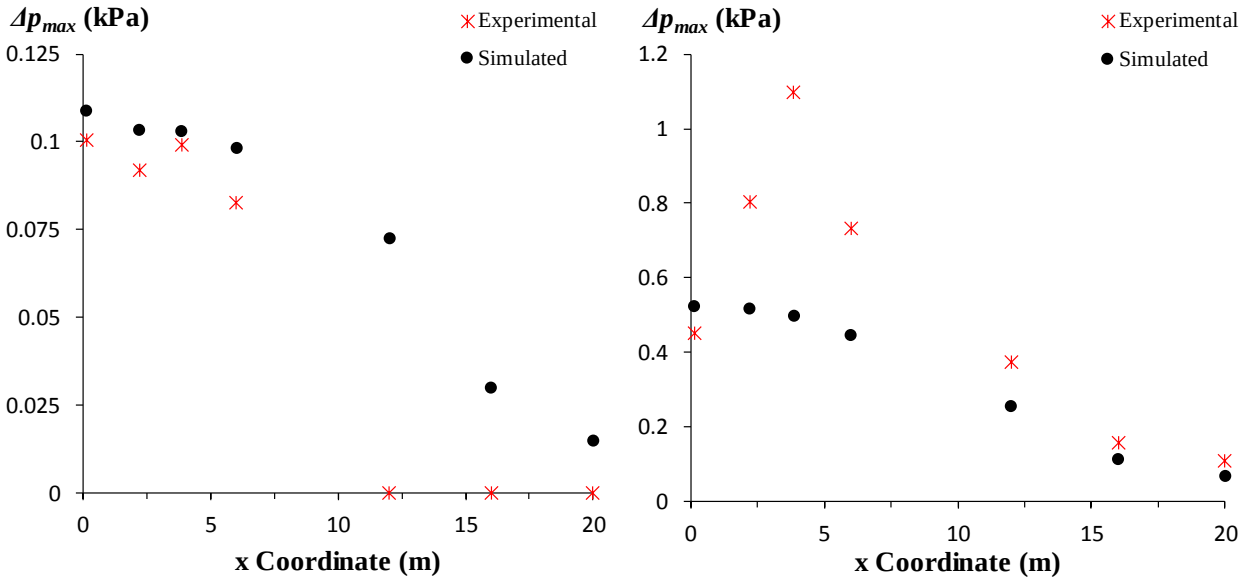

Figure 13: FLACS overpressure predictions compared to experimental results for ammonia/air in the empty (left image) and congested (right image) test configuration.

Figure 14 compares the predicted and measured overpressures for R32/air in both the uncongested and congested configuration. As noted above, there is higher uncertainty in the peak overpressures measured during the empty configuration test as the pressure sensors may have stopped recording before internal pressures reached their peak. Nonetheless, the FLACS results are within a factor of two for the empty test and are much closer for the congested test, for which there is less uncertainty in the measurements.

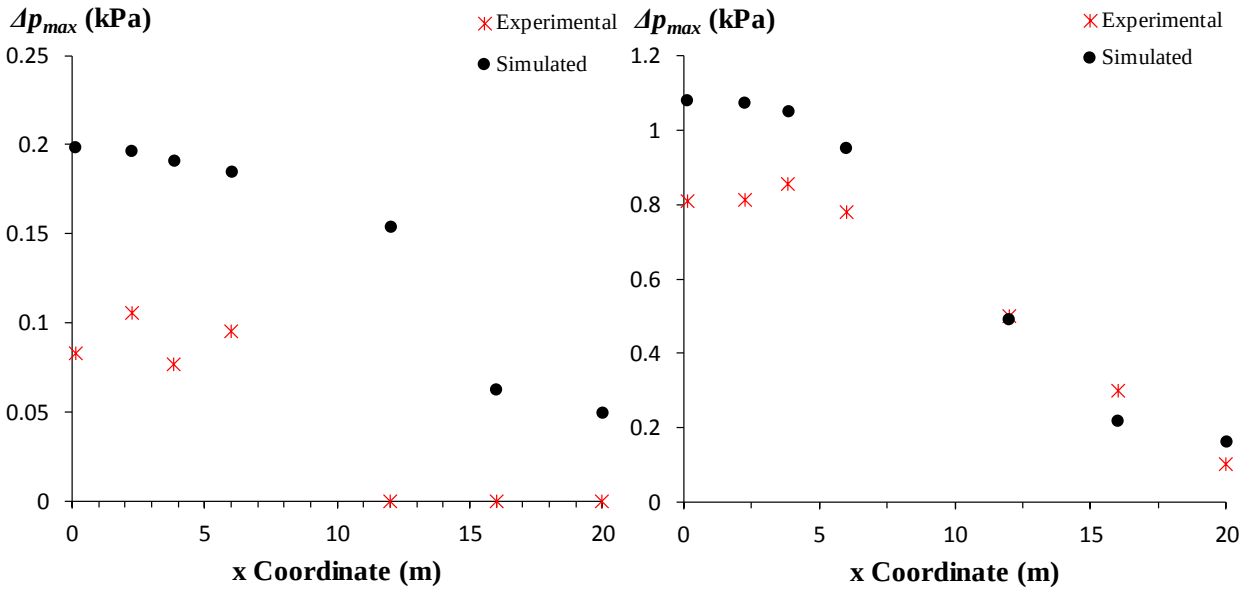

Figure 14: FLACS overpressure predictions compared to experimental results for R32/air in the empty (left image) and congested (right image) test configuration.

FLACS accurately captures both the flame dynamics (e.g., initial buoyancy dominated flame propagation followed by flame accelerations due to the confinement/congestion) as well as the observed overpressures during deflagrations in a partially confined enclosure. Therefore, FLACS was used to evaluate the consequences associated with an unintended release of ammonia in an actual facility setting.

4.4 Practical considerations

If ammonia is unintentionally released and ignited in a partially confined space, the severity could range from negligible overpressures of 0.1 kPa to those orders of magnitude higher. The consequences will be directly related to the degree of confinement and congestion present in and around the vapor cloud and the detailed layout of the facility where the leak occurs. Therefore, when evaluating the explosion consequences of an unintentional release of a low burning velocity fuel such as ammonia, it would not be prudent to assume that there is no risk from such compounds. Conversely, it may be overly conservative to assume the explosion risks of such compounds are close to those of methane. As such, it is necessary to have a tool that can accurately predict both the slow, buoyancy dominated flame propagation as well as the faster flame acceleration caused by confined and congested facilities.

FLACS simulations were run with large ammonia clouds in both a relatively open, yet congested process facility layout and a more confined and congested layout to illustrate how these variables impact the explosion consequences of ammonia. Frames (a), (b), and (c) of Figure 15 show the unconfined scenario, the confined scenario, and the ammonia/air vapor cloud size and location, respectively. The more confined layout included an upper deck to demonstrate the vastly different explosion consequences for the different configurations. In addition, methane vapor clouds were also ignited to demonstrate that assuming methane explosion consequences for ammonia may be overly conservative.

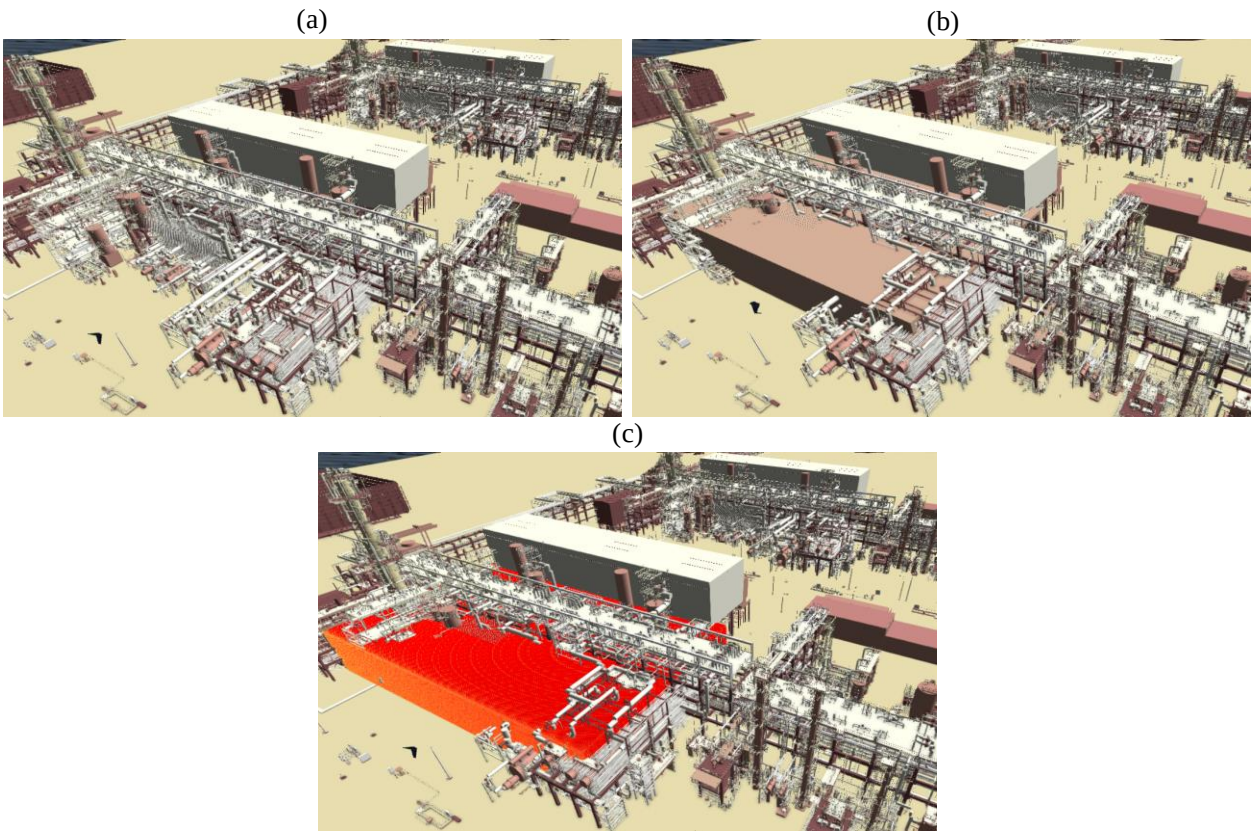

Figure 15: FLACS simulations of ammonia/air and methane air in a generic process facility.

Ignition of the ammonia/air cloud in the unconfined layout resulted in peak overpressures on the order of 0.01 barg. For the scenario with added confinement, peak overpressures were two orders of magnitude higher and close to 0.3 barg. Figure 16 compares the resulting peak overpressures in FLACS for ammonia/air (left frame) and methane/air (right frame), with the color map scale different in each frame. The results show that methane/air vapor cloud explosions have a much higher severity.

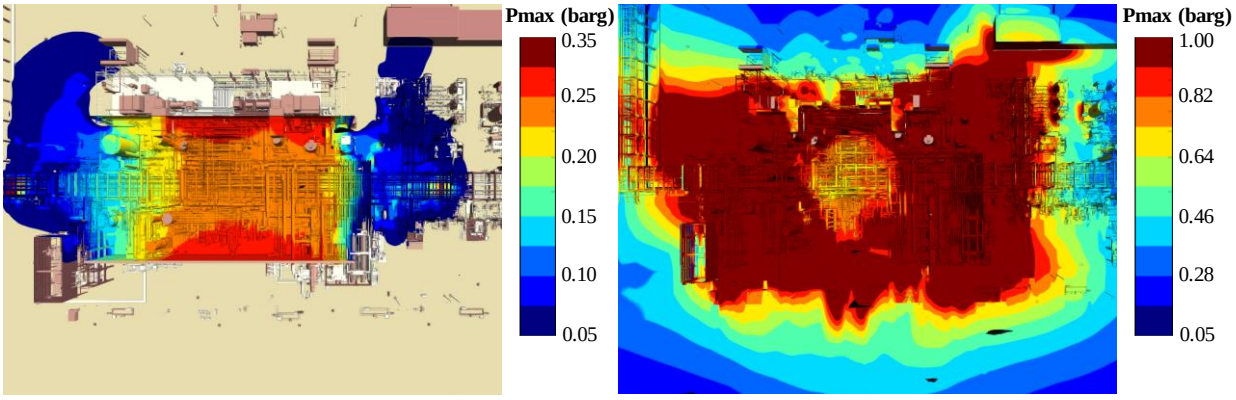

Figure 16: Resulting peak overpressures in FLACS for ammonia/air (left) and methane/air (right) vapor cloud explosions.

Previous ammonia explosions inside buildings, such as cold storage facilities, have caused significant structural damage. While the strength of an external blast wave is highly dependent on the rate at which the fuel/air mixture burns, the pressure rise in an enclosure, such as a building, depends more so on the energy released during combustion and the available venting paths. Internal ammonia deflagrations therefore have non-negligible consequences because the energy release or peak constant volume pressure rise is only slightly lower than that of methane.

To illustrate this, FLACS ignition simulations were performed with stoichiometric ammonia/air and methane/air mixtures partially filling an enclosure. Figure 17 shows the simplified geometry which contains only a refrigerated display case, is completely sealed, and has an internal volume of 66.5 m^3. The figure also shows the prescribed size and position of the stoichiometric clouds, containing 2.2 kg of ammonia and 0.9 kg of methane respectively (same volume and more ammonia because of the higher concentration at stoichiometric conditions). Note that the clouds were positioned at the ceiling because both ammonia and methane are less dense than air.

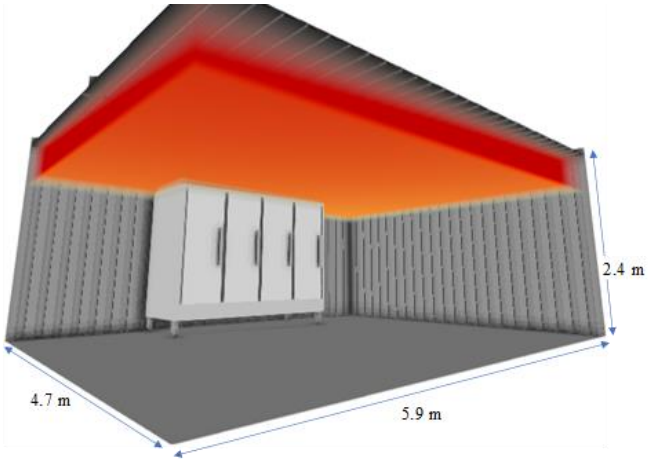

Figure 17: Size and position of stoichiometric ammonia/air and methane/air clouds ignited in an enclosure with FLACS.

Figure 18 provides the predicted overpressures for the ammonia and methane deflagrations. The figure also shows the flame propagation (i.e., the combustion products) at specific times after igniting the ammonia/air mixture (image numbers superimposed on pressure versus time graph). The pressure rise during the ammonia deflagration is more gradual than during the methane deflagration since ammonia has a lower laminar burning velocity. Nonetheless, pressures still reach levels capable of causing structural damage. For releases inside buildings, the peak overpressure will depend largely on the size of the flammable cloud compared to the internal volume of the space, the concentration of ammonia within the cloud, and the potential venting paths such as low strength windows that yield at relatively lower pressures.

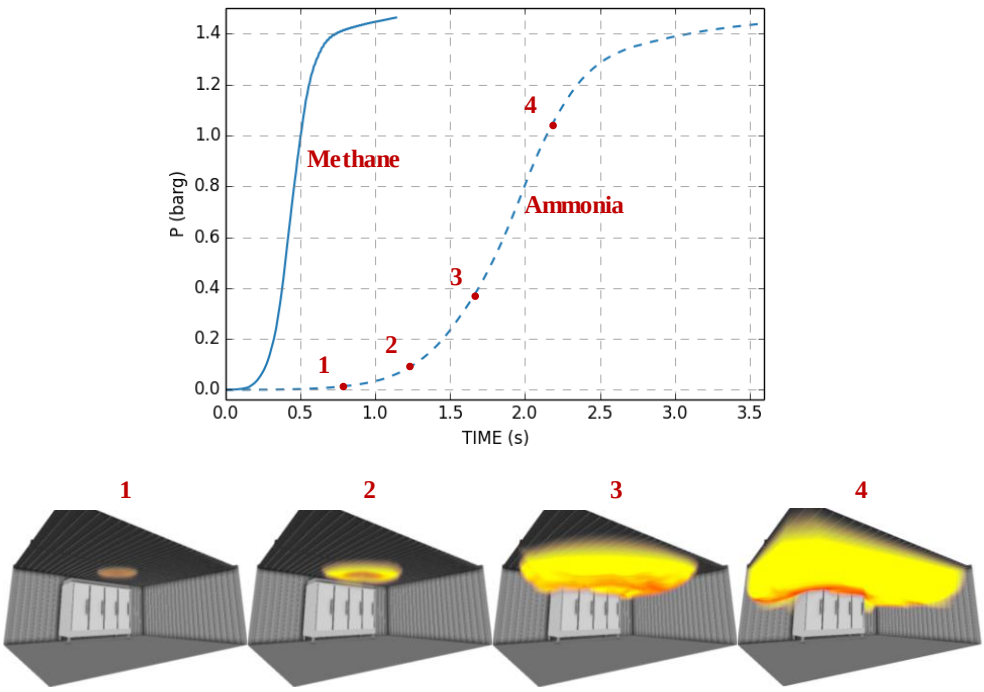

Figure 18: Pressure versus (upper frame) during the ammonia/air and methane/air deflagrations and the corresponding flame propagation during the ammonia/air case.

5 Conclusions

The present study examined the flammability and explosion characteristics of ammonia and R32 as representative low burning velocity fluids and compared the results to those of methane. Lab-scale tests provided flammability limits, auto-ignition temperature, minimum ignition energy, peak constant-volume pressure rise, deflagration index, and laminar burning velocity as a function of equivalence ratio. These properties helped to qualitatively compare risk for high- and low burning velocity compounds, specifically regarding the likelihood of ignition and the relative differences in associated consequences. Large-scale tests in an open-ended 50 m^3 rig quantified the difference in the deflagration severity for near-stoichiometric ammonia/air, R32/air, and methane/air clouds filling the entire enclosure volume. The large-scale data for ammonia and R32 were then compared to FLACS predictions to validate the software for predicting deflagrations involving low burning velocity fluids.

Fundamental combustion properties determined through lab-scale testing were generally in agreement with previously published data, with the exception of MIE, for which large scatter in the data already existed. The LEL, AIT, and MIE of ammonia show that it has a lower likelihood of forming a flammable cloud and of igniting if a flammable cloud forms. The same is true for R32, but potentially to a lesser degree since the AIT is lower than the value for methane.

In the 50 m^3 tests, flame front propagation speeds were much lower for ammonia and R32 compared to methane. The flame dynamics were also much different, with ammonia and R32 flame propagation being buoyancy driven due to the lower laminar burning velocities. In the empty and congested tests, deflagration overpressures were orders of magnitude lower for ammonia/air

and R32/air compared to methane/air. This was consistent with the lower measured values for S_u and K_g.

FLACS simulations captured the buoyancy dominated flame dynamics for the representative mildly flammable fluids and also predicted overpressures close to what was observed in the experiments. Additional simulations of ammonia clouds showed that, under partially and fully confined conditions, ammonia/air vapor cloud explosions can create appreciable overpressures.

The results of the present study show that consequences of low burning velocity fluids, such as ammonia and R32, are lower than methane, but not negligible under certain conditions. Risk assessments must be based on this concept and should incorporate advanced tools to ensure risks are fully apparent and properly mitigated when designing facilities.

6 Acknowledgements

The authors gratefully acknowledge the financial support from Daikin Industries, LTD.

7 References

[1] D. Bjerketvedt, J.R. Bakke and K. Van Wingerden, Gas explosion handbook, Journal of hazardous materials 52 (1997) 1-150.
[2] Determination of Explosion Limits of Gases and Vapours, European Committee for Standardisation, Brussels, Belgium, 2003.
[3] Determination of the Auto Ignition Temperature of Gases and Vapours, European Committee for Standardisation, Brussels, Belgium, 2005.
[4] Standard Test Method for Minimum Ignition Energy and Quenching Distance in Gaseous Mixtures, 2007.
[5] I. Glassman, Combustion, Academic Press, 1997.
[6] K.L. Cashdollar and M. Hertzberg, 20-l explosibility test chamber for dusts and gases, Review of Scientific Instruments 56 (1985) 596-602.
[7] B. Lewis and G. von Elbe, Combustion, Flames, and Explosions of Gases, 1961.
[8] J.L. Pagliaro, G.T. Linteris, P.B. Sunderland and P.T. Baker, Combustion inhibition and enhancement of premixed methane–air flames by halon replacements, Combust. Flame 162 (2015) 41-49.
[9] O.R. Hansen, P. Hinze, D. Engel and S. Davis, Using computational fluid dynamics (CFD) for blast wave predictions, Journal of Loss Prevention in the Process Industries 23 (2010) 885-906.
[10] B.H. Hjertager, Computer simulation of turbulent reactive gas dynamics, Modeling, Identification and Control 5 (1984) 211.
[11] F.H. Harlow and P.I. Nakayama, Turbulence transport equations, Physics of Fluids (1958-1988) 10 (1967) 2323-2332.
[12] R. Abdel-Gayed, D. Bradley and M. Lawes, Turbulent burning velocities: a general correlation in terms of straining rates, Proceedings of the Royal Society of London A: Mathematical, Physical and Engineering Sciences 414 (1987) 389-413.
[13] K.N.C. Bray, Studies of the turbulent burning velocity, Proceedings of the Royal Society of London A: Mathematical, Physical and Engineering Sciences 431 (1990) 315-335.
[14] *International Refrigeration and Air Conditioning Conference*, 2008; Prudue University, Paper 937.

[15] S. Kondo, Y. Urano, K. Takizawa, A. Takahashi, K. Tokuhashi and A. Sekiya, Flammability limits of multi-fluorinated compounds, Fire Safety Journal 41 (2006) 46-56.
[16] P.D. Ronney and H.Y. Wachman, Effect of Gravity on Laminar Premixed Gas Combustion I - Flammability Limits and Burning Velocities, Combust. Flame 62 (1985).
[17] *Symposium (International) on Combustion*, 1967; Elsevier, 985-992.
[18] K. Takizawa, N. Igarashi, S. Takagi, K. Tokuhashi and S. Kondo, Quenching distance measurement of highly to mildly flammable compounds, Fire Safety Journal 71 (2015) 58-68.
[19] T. Jabbour and D. Clodic, Burning Velocity and Refrigerant Flammability Classification, ASHRAE NA-04-1-3 (2004) 522-533.
[20] S. Kondo, K. Takizawa, A. Takahashi and K. Tokuhashi, Measurement and numerical analysis of flammability limits of halogenated hydrocarbons, Journal of hazardous materials 109 (2004) 13-21.
[21] R.G. Richard and I.R. Shankland, Flammability of alternative refrigerants, ASHRAE journal 34 (1992) 20-24.
[22] B.H. Minor, D. Herrmann and R. Gravell, Flammability characteristics of HFO-1234yf, Process Safety Progress 29 (2010) 150-154.
[23] K. Eisazadeh-Far, F. Parsinejad, H. Metghalchi and J.C. Keck, On flame kernel formation and propagation in premixed gases, Combust. Flame 157 (2010) 2211-2221.
[24] K. Takizawa, A. Takahashi, K. Tokuhashi, S. Kondo and A. Sekiya, Burning velocity measurements of nitrogen-containing compounds, Journal of hazardous materials 155 (2008) 144-52.
[25] T. Jabbour, Flammable refrigerant classification based on the burning velocity. Ecoles de Mines de Paris, 2004.
[26] P.D. Ronney, Effect of chemistry and transport properties on near-limit flames at microgravity, Combust. Sci. and Technol. 59 (1988) 123-141.
[27] U.J. Pfahl, M.C. Ross and J.E. Shephard, Flammability Limits, Ignition Energy, and Flame Speeds in H2-CH4-NH3-N2O-O2-N2 Mixtures, Combust. Flame 123 (2000) 140-158.
[28] K. Takizawa, A. Takahashi, K. Tokuhashi, S. Kondo and A. Sekiya, Burning velocity measurement of fluorinated compounds by the spherical-vessel method, Combust. Flame 141 (2005) 298-307.
[29] K. Takizawa, S. Takagi, K. Tokuhashi, S. Kondo, M. Mamiya and H. Nagai, Assessment of Burning Velocity Test Methods for Mildly Flammable Refrigerants, Part 1: Closed-Vessel Method, ASHRAE Transactions 119 (2013) 243-254.
[30] S. Davis, J. Pagliaro, T. Debold, M. van Wingerden and K. van Wingerden, Flammability and explosion characteristics of mildly flammable refrigerants, Journal of Loss Prevention in the Process Industries (2017).